

Effect of deposition temperature on $SrFe_{12}O_{19}$@carbonyl iron core-shell composites as high-performance microwave absorbers

Yuan Liu(刘渊), Rong Li(李茸), Ying Jia(贾瑛), Zhen-Xin He(何祯鑫)

Citation: Chin. Phys. B . 2020, 29(6): 067701 . **doi:** 10.1088/1674-1056/ab81fb
Journal homepage: http://cpb.iphy.ac.cn; http://iopscience.iop.org/cpb

What follows is a list of articles you may be interested in

Refractive index of ionic liquids under electric field: Methyl propyl imidazole iodide and several derivatives

Ji Zhou(周吉), Shi-Kui Dong(董士奎), Zhi-Hong He(贺志宏), Yan-Hu Zhang(张彦虎)

Chin. Phys. B . 2020, 29(4): 047801 . **doi:** 10.1088/1674-1056/ab75cd

Broadband microwave absorption properties of polyurethane foam absorber optimized by sandwiched cross-shaped metamaterial

Long-Hui He(贺龙辉), Lian-Wen Deng(邓联文), Heng Luo(罗衡), Jun He(贺君), Yu-Han Li(李宇涵), Yun-Chao Xu(徐运超), Sheng-Xiang Huang(黄生祥)

Chin. Phys. B . 2018, 27(12): 127801 . **doi:** 10.1088/1674-1056/27/12/127801

Linear and nonlinear optical analysis on semiorganic $_L$-proline cadmium chloride single crystal

Mohd Anis, M I Baig, S S Hussaini, M D Shirsat, Mohd Shkir, H A Ghramh

Chin. Phys. B . 2018, 27(4): 047801 . **doi:** 10.1088/1674-1056/27/4/047801

Optoelectronic and thermoelectric properties of Zintl YLi_3X_2(X=Sb, Bi) compounds through modified Becke—Johnson potential

T Seddik, G Uğur, R Khenata, Ş Uğur, F Soyalp, G Murtaza, D P Rai, A Bouhemadou, S Bin Omran

Chin. Phys. B . 2016, 25(10): 107801 . **doi:** 10.1088/1674-1056/25/10/107801

Preparation of multi-walled carbon nanotube-Fe composites and their application as light weight and broadband electromagnetic wave absorbers

Liu Yuan, Liu Xiang-Xuan, Wang Xuan-Jun

Chin. Phys. B . 2014, 23(11): 117705 . **doi:** 10.1088/1674-1056/23/11/117705

Effect of deposition temperature on $SrFe_{12}O_{19}$@carbonyl iron core–shell composites as high-performance microwave absorbers

Yuan Liu(刘渊)†, Rong Li(李茸), Ying Jia(贾瑛), and Zhen-Xin He(何祯鑫)

Xi'an Research Institute of High Technology, Xi'an 710025, *China*

(Received 16 December 2019; revised manuscript received 24 February 2020; accepted manuscript online 23 March 2020)

The $SrFe_{12}O_{19}$@carbonyl iron (CI) core–shell composites used in microwave absorption are prepared by the metal–organic chemical vapor deposition (MOCVD). The x-ray diffractometer, scanning electron microscope, energy dispersive spectrometer, and vector network analyzer are used to characterize the structural, electromagnetic, and absorption properties of the composites. The results show that the $SrFe_{12}O_{19}$@CI composites with a core–shell structure could be successfully prepared under the condition: deposition temperatures above 180 °C, deposition time 30 min, and gas flow rate 30 mL/min. The electromagnetic properties of the composites change significantly, and their absorption capacities are improved. Of the obtained samples, those samples prepared at a deposition temperature of 180 °C exhibit the best absorption performance. The reflection loss of $SrFe_{12}O_{19}$@CI (180 °C) with 1.5 mm–2.5 mm in thickness is less than −10 dB in a frequency range of 8 GHz–18 GHz, which covers the whole X band and Ku band.

Keywords: $SrFe_{12}O_{19}$, carbonyl iron, electromagnetic properties, microwave absorption

PACS: 77.84.Lf, 78.20.Ci, 62.20.Mm, 81.05.Lg **DOI:** 10.1088/1674-1056/ab81fb

1. Introduction

The combination of different absorbers with complementary performance is one of the effective means to improve the absorption performance.[1] In recent years, core–shell magnetic absorbers have become a research hotspot because of their unique structures and designabilities.[2] According to the actual absorbing effect, the absorbing performance of core–shell magnetic absorber is better than that of single component.[3,4] The results show that the core–shell composite absorbers can not only achieve the absorption performance of core–shell components, but also introduce a lot of interactions between core–shell interface, such as interface polarization and interface coupling, and increase the wave path length of electromagnetic wave in the process of propagation, which will contribute to the absorption of electromagnetic wave.[5]

The $SrFe_{12}O_{19}$ is widely used in microwave area because of many advantages, such as large magnetic anisotropy, high coercive force, and stable chemical properties.[6–8] Carbonyl iron (CI) has been extensively used as an absorption material due to its simple preparation, low cost, large magnetic loss angle, and strong absorption ability.[9–12] The CI presents good dielectric properties at high frequencies, and its content in composite materials can be effectively adjusted to regulate complex permittivity.[13] The research on $SrFe_{12}O_{19}$ coated with micro- and nano-magnetic metals is rare. Pan *et al.*, for instance, coated a series of magnetic metals on the surface of $SrFe_{12}O_{19}$ through electroless plating and found that the properties of the magnetic metals complement the absorption properties of $SrFe_{12}O_{19}$.[14,15] Indeed, the core–shell structure and corresponding interfacial interactions between these components contribute to the composite's absorption of electromagnetic waves.

Despite its great potential, however, electroless plating presents a number of drawbacks, such as complex sensitization, high cost, slow plating speed, and introduction of impurities, such as phosphorus, thus restricting its further application. As an alternative, the metal–organic chemical vapor deposition (MOCVD), a novel chemical vapor deposition (CVD) technology in which organometallic compounds are selected as the material source, presents the following advantages: low deposition temperature; fast and flexible deposition rate, controllable synthetic material composition, and excellent control of the shell thickness, composition, and doping content tuned process parameters.[16,17] In the present experiment, high-purity $Fe(CO)_5$ and $SrFe_{12}O_{19}$ are used as raw materials and high-purity N_2 is used as the carrier gas to synthesize micro- and nano-scale composite absorbents via the MOCVD method. The influence of the CI shell on the crystal structure, morphology, complex permittivity, complex permeability, and microwave absorption properties of the resultant $SrFe_{12}O_{19}$ particles are then investigated.

2. Experiment

2.1. Synthesis of samples

2.1.1. Synthesis of $SrFe_{12}O_{19}$

Stoichiometric amounts of $Sr(NO_3)_2$ and $Fe(NO_3)_3$ were dissolved in distilled water, and an appropriate amount of citric acid (1:1 molar ratio of citric acid to NO_3^-) was added to the mixture to complex the metal ions completely. The pH of the

†Corresponding author. E-mail: liuyuanbixue@163.com

© 2020 Chinese Physical Society and IOP Publishing Ltd

sol was maintained at 7.0 by the slow addition of ammonia solution (25 wt%). The solution was evaporated at 80 °C until a viscous gel formed. The gel was air-dried at 120 °C, ignited in air, and burned into dendritic powders. Finally, the precursor powder was sintered at 1000 °C for 3 h (heating and cooling rate of 5 °C/min, natural cooling after dropping to 300 °C).

2.1.2. MOCVD

Exactly 5-g $SrFe_{12}O_{19}$ powder and 15-mL iron pentacarbonyl $[Fe(CO)]_5$ were added to the reactor and the evaporator, respectively. The N_2 passed through the system to ensure that all of the air in the tube was blown out. Then, the N_2 supply was switched off as the valve between the reactor and the evaporator was closed. The $SrFe_{12}O_{19}$ was heated to 80 °C, and $Fe(CO)_5$ was heated to 160 °C, 180 °C, or 200 °C, and then the valve between the reactor and evaporator was opened while N_2 was steam blown into the reactor (30 mL/min). The reactor was vigorously and continuously stirred mechanically to obtain a uniform coating. The flow of N_2 was controlled by a gas flow meter. An HH-SA digital thermostat oil bath was used to heat the $Fe(CO)_5$. The reactor pipe was coated with an insulating sleeve to prevent the gaseous $Fe(CO)_5$ from condensing at low temperature. The $Fe(CO)_5$ was steam blown into the reactor for 30 min, and the final sample was cooled under an N_2 atmosphere.

2.2. Property measurements

The phase structure of the powders was determined by the x-ray diffraction (XRD; D/max-IIB, Japan). A VEGA II XMU INCA scanning electron microscope (SEM) was employed for morphological analysis. The INCA 7718 spectroscopy (EDS) was employed to analyze the distribution of elements in the sample. Complex permeability and permittivity were measured by using a vector network analyzer (HP-8720ES) in a frequency range of 2 GHz–18 GHz. The samples used for complex permeability and permittivity measurements were prepared by dispersing the powders into paraffin wax at a mass fraction of 60% and then pressing them into a compact toroidal shape with outer and inner diameter of 7.0 mm and 3.0 mm, respectively. The reflection loss of the prepared absorber as a function of frequency was studied by using an HP 8510B vector network analyzer and standard horn antennas in an anechoic chamber.

3. Results and discussion

3.1. XRD analysis

Figure 1 shows the XRD patterns of $SrFe_{12}O_{19}$ and $SrFe_{12}O_{19}$@CI obtained at different deposition temperatures. The characteristic XRD peaks of $SrFe_{12}O_{19}$ are compared with those in the powder diffraction card database (JCPDS 33-1340). The $SrFe_{12}O_{19}$ shows good anastomosis, and no peaks corresponding to impurities were found. The sharp XRD peaks reflecting the crystal plane are found. The relative intensity and crystalline form of the sample are complete, thus indicating that pure $SrFe_{12}O_{19}$ powder is generated. After CI is coated on the surface of $SrFe_{12}O_{19}$, diffraction peaks belonging to $SrFe_{12}O_{19}$ (JCPDS 33-1340) and the α-Fe phase (JCPDS 06-0696) are observed in the samples, thus indicating that besides strontium ferrite and the α-Fe phase, no other impurity phase is generated. As the deposition temperature increases, the characteristic diffraction peaks of $SrFe_{12}O_{19}$ gradually weaken while the (110) crystal plane orientation grows., by using the RIR method of Jade5.0 software the α-Fe relative content values of sample at 160 °C, 180 °C, and 200 °C in the sample relative to α-Fe content of the iron are calculated to be 18%, 20%, and 24%, respectively. This finding indicates that the α-Fe content of the obtained core–shell $SrFe_{12}O_{19}$@CI powders gradually increases as deposition temperature increases.

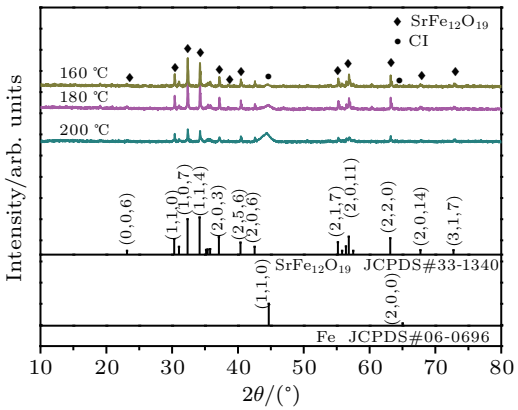


Fig. 1. XRD patterns of $SrFe_{12}O_{19}$ and $SrFe_{12}O_{19}$@CI core–shell powders deposited at different temperatures.

3.2. SEM analysis

The scanning electron microscope micrographs of $SrFe_{12}O_{19}$ and the $SrFe_{12}O_{19}$@CI samples are shown in Fig. 2. Figure 2(a) shows an SEM image of the $SrFe_{12}O_{19}$ powder; here, irregularly shaped platelet-like crystals and smooth surfaces can be observed. The particles of the samples prepared under different temperatures stack on the top of each other due to magnetic attraction and are uniformly coated with Fe as illustrated in Figs. 2(b)–2(d). At a low deposition temperature (160 °C), the $SrFe_{12}O_{19}$ surface reactions proceed slowly, and the gaseous $Fe(CO)_5$ has adequate time to diffuse through the $SrFe_{12}O_{19}$ surface because the deposition process at this time is primarily controlled by surface reactions; thus, gas diffusion presents minimal effects. At this point, the nucleation rate is greater than the nucleus growth rate. Hence, the CI on the surface of $SrFe_{12}O_{19}$ is uniformly fine but fails to form a complete surface coating. When a small amount of $Fe(CO)_5$ vapor is added to the reaction system, the CI particles with average diameters of approximately 200 nm–300 nm are found

in some of the $SrFe_{12}O_{19}$ particles (Fig. 2(b)). As the deposition temperature increases (180 °C), the surface reaction rate increases. At this point, deposition is mainly controlled by gas diffusion, and CI particles begin to gather and agglomerate because the nucleation rate is lower than the nucleus growth rate. As the CI content added to the reaction system increases, the particles become coralloid in shape, and their arris disappears due to the increasing of the thickness of the CI shells. A complete $SrFe_{12}O_{19}$@CI core–shell structure is subsequently formed. When the deposition temperature increases to 200 °C, part of the reacting gas initiates new reactions on the surface of the shell, resulting in the some CI particles disappearing from the shell surface (Fig. 2(d)).

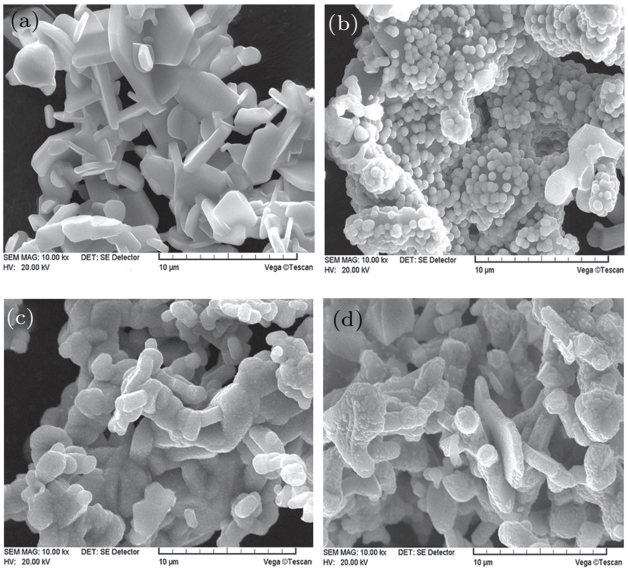


Fig. 2. SEM photograph of (a) $SrFe_{12}O_{19}$, and that of $SrFe_{12}O_{19}$@CI core–shell powders deposited at (b) 160 °C, (c) 180 °C, and (d) 200 °C.

Direct observation of the CI shell is performed by cold mounting samples (180 °C, 30 min, 30 mL/min) in epoxy, followed by sanding and polishing. The SEM was then used to observe the cross sections of the samples. Figure 3(a) shows that the $SrFe_{12}O_{19}$ particles are coated with a layer of continuous white material, and the average thickness, which is measured by using an electronic ruler, is approximately 0.5 μm. Figure 3(b) shows an EDS scan of the spot marked as A in the cross section of the sample. The obtained spectrum confirms the presence of elemental Fe, which indicates that the white material is CI.

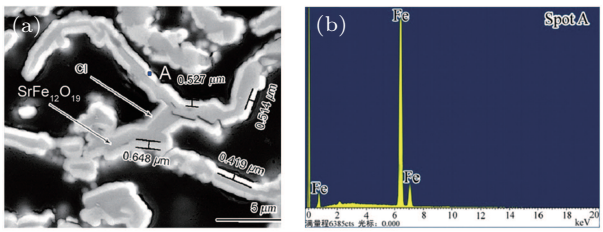


Fig. 3. (a) SEM and (b) EDS spectrum of $SrFe_{12}O_{19}$@CI cross-section.

3.3. Complex permittivity and permeability

Figure 4 shows the complex permittivity and permeability of pure $SrFe_{12}O_{19}$ and $SrFe_{12}O_{19}$@CI composites prepared at different deposition temperatures. Figures 4(a) and 4(b) respectively show the real (ε') and imaginary (ε'') parts of the permittivity of the specimens plotted as a function of frequency. The ε' and ε'' of the specimen remain relatively constant with only slight fluctuations over the entire frequency range studied but increase withg deposition temperature increasing. According to these results, the α-Fe content of the composite powders increases as the temperature increases, thus forming a surface layer; hence, the conductivity and permittivity of the samples remarkably increase. Due to the metallic properties of the shell, electrons can travel freely and accumulate at the $SrFe_{12}O_{19}$@CI interface to form a structure similar to a boundary–layer capacitor to generate interfacial electric dipolar polarization. Complex permittivity is usually derived from electronic polarization, ionic polarization, electric dipole polarization, and interfacial polarization. The electron and ion polarizations only occur at frequencies higher than those of the infrared range.[18] Hence, the complex permittivity observed in the present samples can be mainly attributed to the increases in their electric dipole and interfacial polarization. Electrons transfer freely to the surface layer and accumulate at the interface between CI and $SrFe_{12}O_{19}$ to form a border capacitor and generate electric dipole polarization due to CI shell formation. The core–shell structure also increases the sample interfacial polarization, which, in turn, increases the complex permittivity of $SrFe_{12}O_{19}$@CI.

The plots of real (μ') and imaginary (μ'') parts of the permeability of the specimens are shown in Figs. 4(c) and 4(d), respectively. The permeability values of the coated sample are remarkably improved compared with that of the original $SrFe_{12}O_{19}$. The μ' values of the coated samples slowly decrease as frequency increases, and higher μ' values are found in $SrFe_{12}O_{19}$@CI composites with higher CI content values. By contrast, the μ'' values of the coated samples are basically maintained at a constant value and decrease with CI content increasing. The soft magnetic α-Fe phase is isolated by the hard magnetic $SrFe_{12}O_{19}$ phase in the $SrFe_{12}O_{19}$@CI core–shell composites, thereby reducing the eddy current loss of α-Fe at high frequency. Moreover, nanocomposites possess sufficient exchange coupling, and small size effect, which leads the domain wall displacement to decrease, and the magnetic loss to increase. As the α-Fe content of the sample increases, the soft-soft interaction is enhanced, but the interaction between the soft magnetic α-Fe and hard magnetic $SrFe_{12}O_{19}$ is suppressed, thus reducing the exchange coupling and μ''.

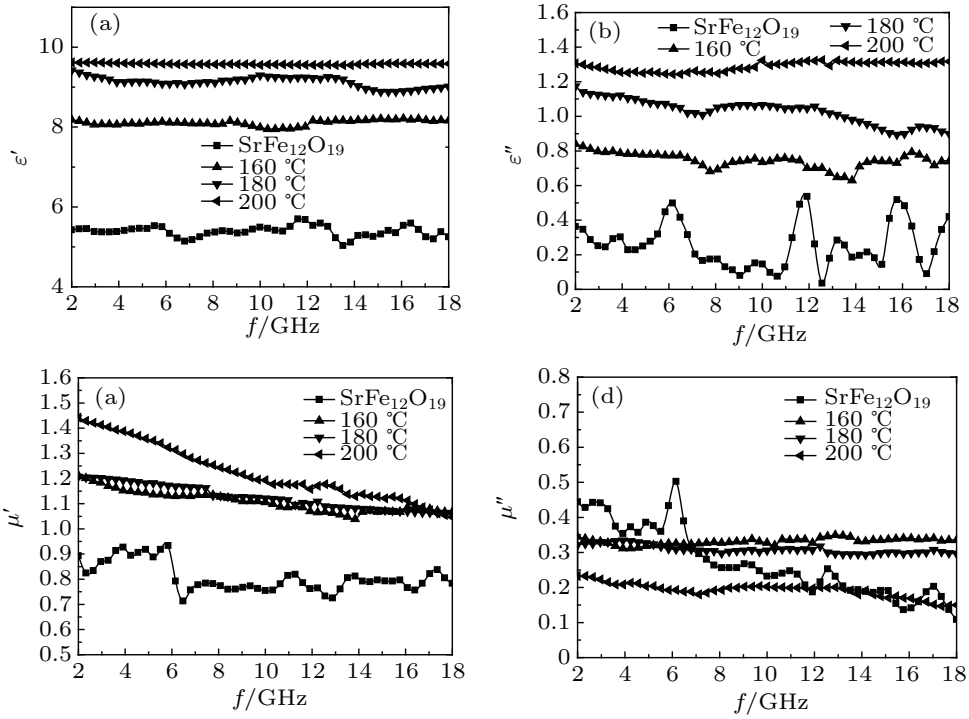


Fig. 4. Electromagnetic parameters of $SrFe_{12}O_{19}$ and the $SrFe_{12}O_{19}$@CI core–shell powders deposited at different temperatures.

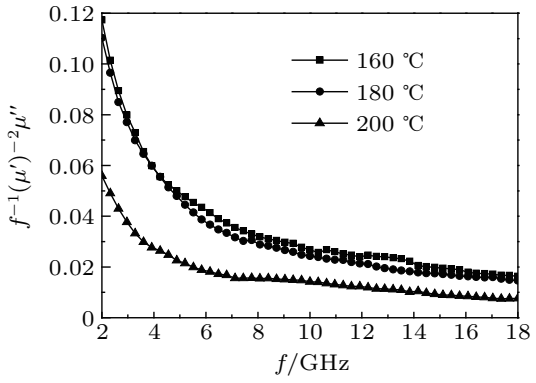


Fig. 5. Plots of $f^{-1}(\mu')^{-2}\mu''$ *versus* frequency of $SrFe_{12}O_{19}$@CI.

At microwave frequencies, the dielectric loss of material comes from their own polarization and interfacial polarization. The $SrFe_{12}O_{19}$ with a large number of CI interfaces can achieve high interfacial polarization and thus enhancing the dielectric loss. A general loss of microwave magnetic material mainly comes from the eddy current loss, magnetization vector rotation, natural resonance, and magnetic domain wall resonance.[19] Magnetization vector rotation only occurs under a strong magnetic field, and the contribution of magnetic domain wall resonance to the microwave frequency is negligible.[20] Therefore, the electromagnetic wave loss of $SrFe_{12}O_{19}$@CI is mainly caused by eddy current loss or natural resonance. The eddy current loss depends on the thickness (d) and conductivity (σ) of a material and can be expressed as follows:[21]

$$\mu'' \cdot (\mu')^2 f^{-1} \approx 2/3\pi\mu_0 d^2\sigma,$$

where μ_0, d, c, and f are the vacuum permeability, thickness, velocity of light in free space, and frequency of electromagnetic wave in free space, respectively. If the $SrFe_{12}O_{19}$@CI experiences magnetic loss from only the eddy current loss, $f^{-1}(\mu')^{-2}\mu''$ should be constant. Figure 5 shows the values of $f^{-1}(\mu')^{-2}\mu''$ as a function of the frequency of $SrFe_{12}O_{19}$@CI. A downward trend can be observed as the frequency increases. Hence, the $SrFe_{12}O_{19}$@CI magnetic loss is mainly dominated by natural resonance at 2 GHz–8 GHz, while eddy current loss exists at 8 GHz–18 GHz.

3.4. Microwave absorption properties

Absorbing materials must meet two conditions: (i) electromagnetic wave (EMW) must penetrate into the interior of material as extensively as possible and (ii) the material must be able to consume the incoming electromagnetic wave, which has a large attenuation constant.[22] Figure 6 shows the sample dielectric losses ($\tan\delta_\varepsilon$) and magnetic losses ($\tan\delta_\mu$), which contribute to microwave absorption ($\tan\delta = \tan\delta_\varepsilon + \tan\delta_\mu$, $\tan\delta_\varepsilon = \varepsilon''/\varepsilon'$, $\tan\delta_\mu = \mu''/\mu'$). The dielectric loss increases with CI content increasing. Such increases obviously result from the formation of CI shell on the surface of the $SrFe_{12}O_{19}$ core. In contrast to the dielectric loss, the magnetic loss shows the opposite trend. Improvement in the microwave absorption of the $SrFe_{12}O_{19}$@CI composites originates from the efficient combination of $SrFe_{12}O_{19}$ and CI. In general, the microwave absorption of a material is related to the balance between tan δ_ε and tan δ_μ. It is the best that the tan δ_ε and tan δ_μ are close to each other (Fig. 6(c)), so the impedance matching performance is good, which is conducive to the absorption of EMWs.

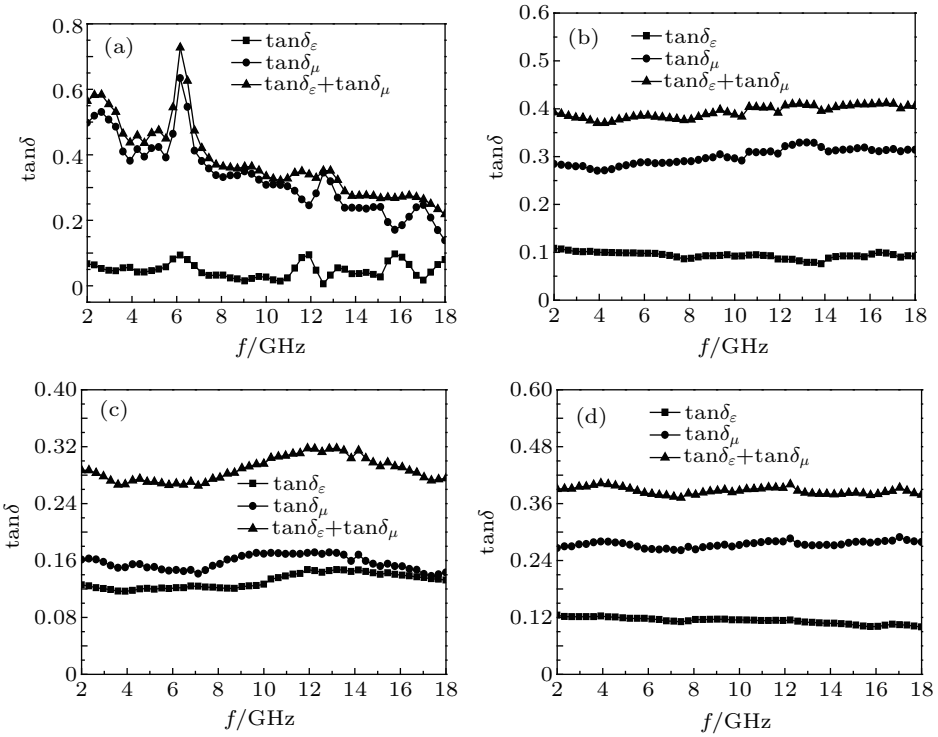


Fig. 6. Dielectric and magnetic loss factors of (a) $SrFe_{12}O_{19}$ and $SrFe_{12}O_{19}$@CI deposited at (b) 160 °C, (c) 180 °C, and (d) 200 °C.

The EMWs entering into a material should be nearly completely attenuated (attenuation characteristic) to achieve low reflection. The attenuation constant (α) can be expressed as follows:[23]

$$\alpha = \sqrt{2}\pi f \times \sqrt{(\mu''\varepsilon'' - \mu'\varepsilon') + \sqrt{(\mu''\varepsilon'' - \mu'\varepsilon')^2 + (\varepsilon'\mu'' - \mu'\varepsilon'')^2}}\Big/c.$$

The attenuation constants of the $SrFe_{12}O_{19}$ and $SrFe_{12}O_{19}$@CI particles deposited at different temperatures are shown in Fig. 7. After the CI shell is grown on the surface of $SrFe_{12}O_{19}$, the attenuation constant of the sample increases significantly. Hence, the absorption performance of $SrFe_{12}O_{19}$@CI is better than that of pure $SrFe_{12}O_{19}$. Of the samples obtained, he sample deposited at 180 °C shows the best absorption effect.

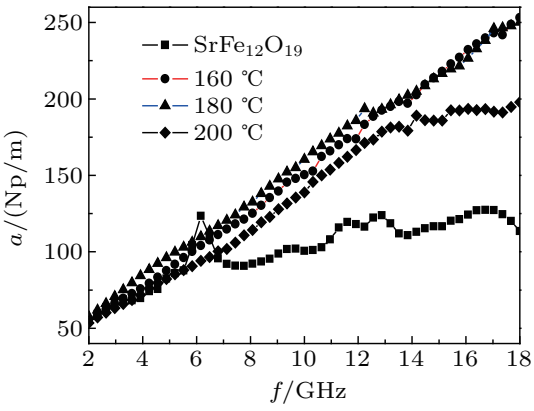


Fig. 7. Attenuation constants of $SrFe_{12}O_{19}$ and $SrFe_{12}O_{19}$@CI.

The EMWs reflection loss is calculated by using the transmission line theory,[24,25] which is expressed as follows:

$$RL = -20\lg\left|\frac{Z_{\text{in}} - Z_0}{Z_{\text{in}} + Z_0}\right|, \tag{1}$$

$$Z_{\text{in}} = Z_0\left(\frac{\mu_{\text{r}}}{\varepsilon_{\text{r}}}\right)^{1/2}\tanh\left(\frac{\text{j}2\pi d f\sqrt{\varepsilon_{\text{r}}\mu_{\text{r}}}}{c}\right), \tag{2}$$

where Z_{in} is the normalized input impedance of a metal-backed microwave absorption layer, $Z_0 = 377\ \Omega$ is the intrinsic impedance of free space, ε_{r} and μ_{r} are the relative complex permittivity and permeability, respectively, f is the frequency of the EMW, d is the thickness of the absorber, and c is the velocity of light in vacuum.

In order to make a comparison of microwave absorption properties among CI (The electromagnetic parameters of CI are shown in Ref. [9]), $SrFe_{12}O_{19}$ and $SrFe_{12}O_{19}$@CI (deposited at 180 °C) core–shell composites' powder, the microwave absorption properties of the three samples are investigated by using formulas (1) and (2), and the results are shown in Fig. 8.

It can be concluded from Fig. 8(a) that a better absorption effect of $SrFe_{12}O_{19}$ absorbent with a thickness of 5 mm or more is achieved. Figure 8(b) shows that the reflection peak moves to the low frequency as the absorbent CI coating thickness increases, with minimum reflectance peak −14.6 dB at a thickness of 1 mm, of which the frequency width less than

−10 dB reaches 4 GHz. When the minimum reflectance is −25.0 dB with a thickness of 2 mm, the frequency width less than −10 dB reaches just 2 GHz. Therefore, Simply using the absorber with CI or $SrFe_{12}O_{19}$ is difficult to satisfy the "thin, wide," the requirements for the absorbing material. By contrast, the matching thickness of $SrFe_{12}O_{19}$@CI significantly decreases and absorbing effect is significantly improved (Fig. 8(c)).

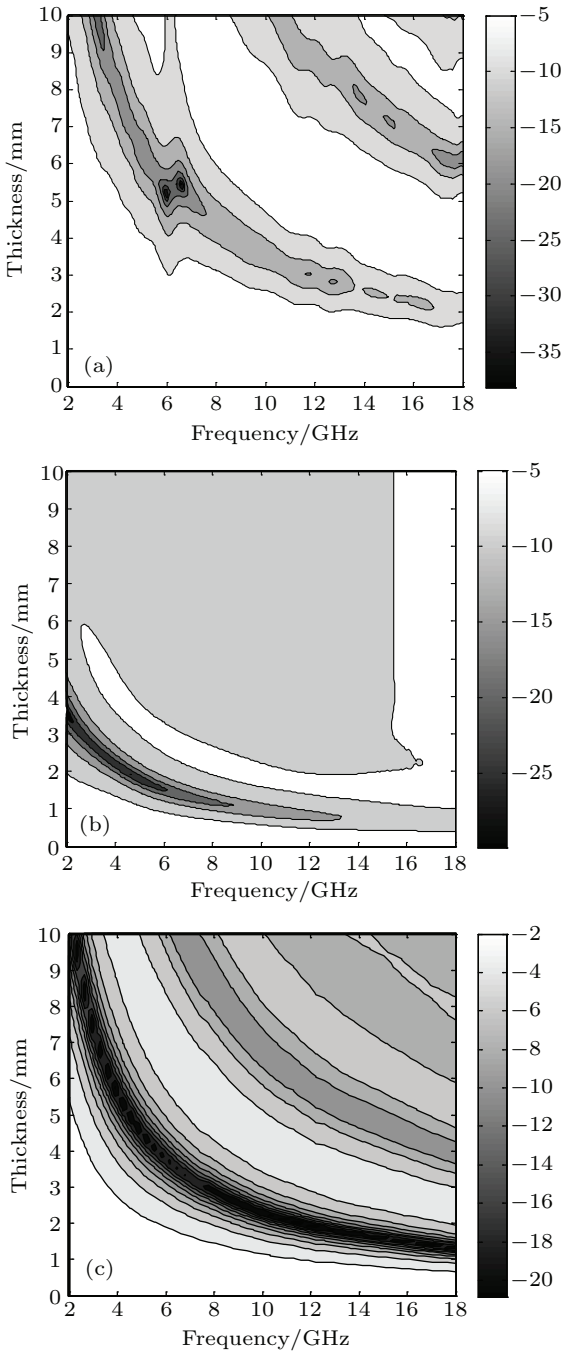


Fig. 8. Microwave absorption properties of (a) $SrFe_{12}O_{19}$, (b) CI, and (c) $SrFe_{12}O_{19}$@CI (180 °C) with different thickness values.

The relationship between the layer thickness and frequency of sample is investigated, and the results are shown in Fig. 9. As the layer thickness increases, the reflectance peak gradually moves toward lower frequencies. The peak reflections first decrease and then increase, and the minimum reflection (−21.2 dB) is obtained at a thickness of 2.0 mm. The reflection loss of $SrFe_{12}O_{19}$@CI (1.5 mm–2.5 mm in thickness) is less than −10 dB in a frequency range of 8 GHz–18 GHz, which covers the whole X band and Ku band.

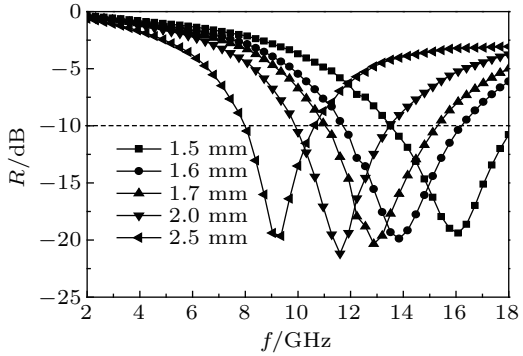


Fig. 9. Microwave absorption properties of $SrFe_{12}O_{19}$@CI (180 °C) with thickness of 1.5 mm–2.5 mm.

3.5. Microwave absorption mechanism

The CI shell grown on the $SrFe_{12}O_{19}$ surface forms a complete core–shell structure, which effectively improves the absorption performance of the $SrFe_{12}O_{19}$. After the EMW incident absorption coating, multiple reflections are formed between absorbing agents, and the electromagnetic loss of the $SrFe_{12}O_{19}$@CI composite is effectively enhanced due to interfacial polarization and natural resonance (Fig. 10(a)). Moreover, the core–shell structure effectively increases the propagation of electromagnetic waves in the interiors of single $SrFe_{12}O_{19}$@CI particles. Multiple reflections between core–shell interfaces can effectively improve electromagnetic wave attenuation (Fig. 10(b)).

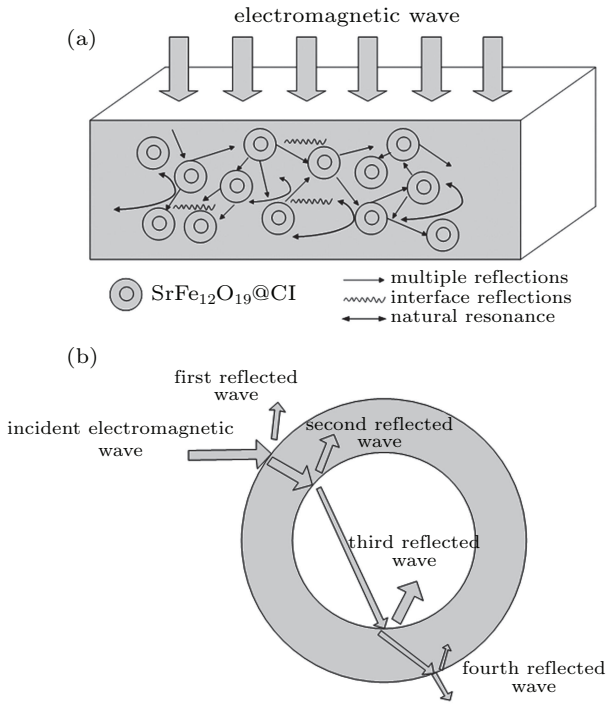


Fig. 10. Schematic diagram of microwave absorption mechanism of $SrFe_{12}O_{19}$@CI composites.

4. Conclusions

The $SrFe_{12}O_{19}$@CI composites are successfully prepared and characterized by MOCVD. XRD, SEM. The EDS shows that uniform CI films can be formed on an $SrFe_{12}O_{19}$ surface. The $SrFe_{12}O_{19}$@CI composite powders with a core–shell structure are successfully prepared under the condition: deposition temperatures above 180 °C, deposition time 30 min, and gas flow rate 30 mL/min. After the CI shell is deposited on the $SrFe_{12}O_{19}$ surface, the electromagnetic parameters of the resulting material show significant changes. The enhanced interfacial interactions between $SrFe_{12}O_{19}$ and CI can provide high electric dipole and interfacial polarization, thereby enhancing the dielectric loss of the composite, and the magnetic loss of $SrFe_{12}O_{19}$@CI composites is mainly attributed to the natural resonance (2 GHz–8 GHz) and eddy current loss (8 GHz–18 GHz). The $SrFe_{12}O_{19}$@CI composites exhibit excellent microwave absorption properties in a frequency range of 2 GHz–18 GHz. Of the samples obtained, the sample prepared at a deposition temperature of 180 °C shows the best absorption effect. The reflection loss of $SrFe_{12}O_{19}$@CI (180 °C) is less than −10 dB in a frequency range of 8 GHz–18 GHz with 1.5 mm–2.5 mm in thickness, which covers the whole X band and Ku band.

References

[1] Liu Y, Liu X X, H E C P and Wang W 2018 *Surf. Technol.* **47** 72 (in Chinese)

[2] Yu J Y, Chi F L, Sun Y P, Guo J J and Liu X G 2018 *Ceram. Int.* **44** 19207

[3] Liu X G, Cui C Y, Yu J Y, Sun Y P and Xia A L 2018 *Mater. Lett.* **225** 1

[4] Liu X G, Yu J Y, Cui C Y, Sun Y P, Li X L and Li Z X 2018 *J. Phys. D: Appl. Phys.* **51** 265002

[5] Liu X G, Ran S L, Yu J Y and Sun Y P 2018 *J. Alloys Compd.* **765** 943

[6] Bobzin K, Bolelli G, Bruehl M, Hujanen A, Lintunen P, Lisjak D, Gyergyek S and Lusvarghi L 2011 *J. Eur. Ceram. Soc.* **31** 1439

[7] Sachin T, Himanshu B B, Ramesh C A, Vijaya A and Trilok C S 2011 *Trans. Indian Inst. Met.* **64** 607

[8] Chen W, Liu Q Y, Zhu X X and Fu M 2017 *RSC Adv.* **7** 40650

[9] Liu Y, Liu X X and Wang X J 2014 *J. Alloys Compd.* **584** 249

[10] Liu Y, Liu X X, Li R and Li Y 2015 *RSC Adv.* **5** 18660

[11] Zhou Y Y, Xie H, Zhou W C and Ren Z W 2018 *J. Magn. Magn. Mater.* **446** 143

[12] Zuo Y X, Yao Z J, Lin H Y, Zhou J T, Guo X L and Cai H S 2019 *J. Mater. Sci.* **54** 11827

[13] Cheng Y L, Dai J M, Wu D J and Sun Y P 2010 *J. Magn. Magn. Mater.* **322** 97

[14] Pan X, Qiu J and Gu M 2007 *J. Mater. Sci.* **42** 2086

[15] Pan X, Shen H, Qiu J and Gu M Y 2007 *Mater. Chem. Phys.* **101** 505

[16] Wang R, Wan Y Z, He F, Qi Y, You W and Luo H L 2012 *Appl. Surf. Sci.* **258** 3007

[17] Manasevit H M 1968 *Appl. Phys. Lett.* **12** 156

[18] Lacrevaz T, Fléchet B, Farcy A, Torres J, Gros-Jean M, Bermond C, VoaO.Cueto T T, Blampey B, Angénieux G, Piquet J and Crécy de F 2006 *Microelectron. Eng.* **83** 2184

[19] Jian Z and Bo C 2017 *J. Mater. Sci. - Mater. Electron.* **28** 1

[20] Iqbal N, Wang X, Babar A A, Zainab G, Yu J and Ding B 2017 *Sci. Rep.* **7** 15153

[21] Li G M, Wang C L, Li W X, Ding R M and Xu Y 2014 *Phys. Chem. Chem. Phys.* **16** 12385

[22] Qing Y, Zhou W, Luo F and Zhu D M 2010 *Carbon* **48** 4074

[23] Zeng M, Zhang X X, Yu R H, Zhao D L, Zhang Y H and Wang X L 2014 *Mater. Sci. Eng. B* **185** 21

[24] Naito Y and Suetake K 1971 *IEEE Trans. Microwave Theory Tech.* **19** 65

[25] Meshram M R, Agrawal N K, Bharoti Sinha and Misra P S 2004 *J. Magn. Magn. Mater.* **271** 207